

# **Turbulence Measurements from Compliant Moorings - Part II: Motion**

## **Correction**

Levi F. Kilcher\*

*National Renewable Energy Laboratory, Golden, Colorado, USA*

Jim Thomson

*Applied Physics Laboratory, University of Washington, Seattle, Washington, USA*

Samuel Harding

*Pacific Northwest National Laboratory, Richland, Washington, USA*

Sven Nylund

*Nortek AS, Norway*

\* *Corresponding author address:* Levi Kilcher, National Renewable Energy Laboratory, 15013 Denver West Pkwy, Golden, Colorado, USA

E-mail: Levi.Kilcher@nrel.gov

## ABSTRACT

14     Acoustic Doppler velocimeters (ADV) are a valuable tool for making high-  
15     precision measurements of turbulence, and moorings are a convenient and  
16     ubiquitous platform for making many kinds of measurements in the ocean.  
17     However—because of concerns that mooring motion can contaminate tur-  
18     bulence measurements and acoustic Doppler profilers are relatively easy to  
19     deploy—ADV are not frequently deployed from moorings. This work de-  
20     tails a method for measuring turbulence using moored ADVs that corrects  
21     for mooring motion using measurements from inertial motion sensors. Three  
22     distinct mooring platforms were deployed in a tidal channel with inertial-  
23     motion-sensor-equipped ADVs. In each case, the motion correction based on  
24     the inertial measurements dramatically reduced contamination from mooring  
25     motion. The spectra from these measurements have a shape that is consistent  
26     with other measurements in tidal channels, and have a  $f^{-5/3}$  slope at high  
27     frequencies—consistent with Kolmogorov’s theory of isotropic turbulence.  
28     Motion correction also improves estimates of cross-spectra and Reynold’s  
29     stresses. Comparison of turbulence dissipation with flow speed and turbu-  
30     lence production indicates a bottom boundary layer production-dissipation  
31     balance during ebb and flood that is consistent with the strong tidal forcing  
32     at the site. These results indicate that inertial-motion-sensor-equipped ADVs  
33     are a valuable new tool for measuring turbulence from moorings.

## 34 1. Introduction

35 Acoustic Doppler velocimeters (ADV) have been used to make high-precision measurements of  
36 water velocity for over 20 years (Kraus et al. 1994; Lohrmann et al. 1995). During that time, they  
37 have been deployed around the world to measure turbulence from a range of platforms, including  
38 stationary structures on ocean- and lake-bottoms, in surface waters from a pole lowered from  
39 a ship’s bow, and in the deep ocean from autonomous underwater vehicles (e.g., Voulgaris and  
40 Trowbridge 1998; Zhang et al. 2001; Kim et al. 2000; Goodman et al. 2006; Lorke 2007; Geyer  
41 et al. 2008; Cartwright et al. 2009).

42 A relatively small fraction of ADV measurements have been made from moorings (e.g., Fer  
43 and Paskyabi 2014). Presumably this is because mooring motion can contaminate ADV mea-  
44 surements, and acoustic Doppler profilers (ADPs) can be used to measure mid-depth turbulence  
45 statistics without a mooring (e.g., Stacey et al. 1999a; Rippeth et al. 2002; Wiles et al. 2006).  
46 Still, ADV measurements have distinct characteristics that can be advantageous: they are capa-  
47 ble of higher sample rates, have higher signal-to-noise ratios, and have a much smaller sample  
48 volume (1 centimeter, as opposed to several meters). That is, compared to an ADP, ADVs are  
49 high-precision instruments capable of providing unique information. They could be more widely  
50 used as a moored instrument (i.e., at an arbitrary depth) if a method for accounting for mooring  
51 motion can be demonstrated to provide more accurate estimates of turbulence statistics.

52 Inertial motion unit (IMU) sensors have been used in the aerospace and aeronautical industries  
53 to quantify the motion of a wide range of systems, and to improve atmospheric velocity measure-  
54 ments, for several decades (Axford 1968; Edson et al. 1998; Bevly 2004). Over the last 10 years,  
55 the smartphone, drone, and ‘Internet of Things’ markets has driven innovation in microelectrical-  
56 mechanical systems, including the IMU. As a result of this growth and innovation the cost, power

57 requirements, and size of IMUs have come down. These changes have allowed these sensors to be  
58 integrated into oceanographic instruments that have small form-factors, and rely on battery power.

59 Nortek now offers a version of their Vector ADV with a Microstrain 3DM-GX3-25 IMU sensor  
60 (Nortek 2005; MicroStrain 2012). This IMU's signals are incorporated into the Vector data stream  
61 so that its motion and orientation signals are tightly synchronized with the ADV's velocity mea-  
62 surements. This tight synchronization provides a data stream that can be utilized to quantify ADV  
63 motion in the Earth's inertial reference frame, and remove that motion from the ADV's velocity  
64 measurements at each time step of its sampling (Edson et al. 1998). This work utilizes moored  
65 'ADV-IMU' measurements from mid-depths in Puget Sound to demonstrate that motion correc-  
66 tion can improve the accuracy of oceanic turbulence spectra, turbulence dissipation, and Reynolds  
67 stress estimates from moored platforms.

68 This effort was originally motivated by a need for low-cost, high-precision turbulence measure-  
69 ments for the emerging tidal energy industry (McCaffrey et al. 2015; Alexander and Hamlington  
70 2015). Experience in the wind energy industry has shown that wind turbine lifetime is reduced by  
71 atmospheric turbulence, and the same is expected to be true for tidal energy turbines. In wind, me-  
72 teorological towers are often used to position sonic anemometers at the hub height of wind turbines  
73 for measuring detailed turbulence inflow statistics (Hand et al. 2003; Kelley et al. 2005; Mücke  
74 et al. 2011; Afgan et al. 2013). In the ocean, tower-mounted hub-height turbulence measurements  
75 have been made, but they are challenging to install and maintain in energetic tidal sites (Gunawan  
76 et al. 2014; Thomson et al. 2012). Therefore, the U.S. Department of Energy funded this work to  
77 investigate the accuracy of mooring-deployed ADV-IMUs to reduce the cost of turbulence mea-  
78 surements at tidal energy sites (Kilcher et al. 2016). The approach proved to be successful and  
79 potentially useful to the broader oceanographic community interested in moored turbulence mea-

80 surements (Lueck and Huang 1999; Doherty et al. 1999; Nash et al. 2004; Moum and Nash 2009;  
81 Alford 2010; Paskyabi and Fer 2013).

82 The next section describes details of the measurements, including a summary of the hardware  
83 configurations (platforms) that were used to support and position the ADV-IMUs in the water  
84 column. A detailed description of the motion of these platforms is found in the companion paper to  
85 this work, Harding et al. (in review), hereafter Part 1. Section 3 describes the mathematical details  
86 of motion correction and Section 4 presents results from applying the method to measurements  
87 from the various platforms. Section 5 is a discussion of the energetics of the tidal channel in  
88 which the measurements were made and demonstrates that the measurements are consistent with  
89 turbulence theory and other measurements in similar regimes. A summary and concluding remarks  
90 are provided in Section 6.

## 91 **2. Measurements**

92 This work focuses on measuring turbulence from ADVs that are equipped with IMUs and de-  
93 ployed from moving (moored) platforms. The ADVs utilized for these measurements were Nortek  
94 Vector ADVs equipped with Microstrain 3DM-GX3-25 IMU sensors. These IMUs captured all  
95 six components of the ADV motion (three components of angular rotation and three components  
96 of linear acceleration), as well as the orientation of the ADV pressure case. The sampling of the  
97 motion sensor is tightly synchronized with the ADV measurements. The IMU measures its mo-  
98 tion at 1 kHz and uses internal signal integration (Kalman filtering) to output the motion signals  
99 at the same sample rate as the ADV's velocity measurements. This reduces aliasing of the IMU's  
100 motion measurements above the ADV's sample rate (MicroStrain 2010). Cable-head ADVs were  
101 used throughout this work to allow for flexibility in the positioning of the ADV head relative to its  
102 pressure case.

103 All measurements used in this work were made in Admiralty Inlet, Washington, approximately  
104 500 m west southwest of Admiralty Head in 60-m of water near 48° 9.18' N, 122° 41.22' W  
105 (Figure 1). The site is approximately 6 km east of Port Townsend, and 1 km north of the Port  
106 Townsend to Coupeville ferry route. Admiralty inlet is the largest waterway connecting Puget  
107 Sound to the Strait of Juan de Fuca, and it possesses a large semidiurnal tidal flow (Thomson  
108 et al. 2012; Polagye and Thomson 2013). This work utilizes data from three distinct deployment  
109 platforms: the tidal turbulence mooring, a StableMoor buoy, and a simple sounding weight. All  
110 data used in this analysis is available from the MHK data repository (<http://mhkdr.openei.org>;  
111 submission ids: 49, 50 and 51). Additional details, photos, and schematic diagrams of all three  
112 mooring systems can be found in Part 1.

### 113 *a. Tidal Turbulence Mooring*

114 The tidal turbulence mooring (TTM) is a simple mooring system with a strongback fin sus-  
115 pended between a steel clump-weight anchor weighing 1,200 kg when dry and a 0.93-m-diameter  
116 spherical steel buoy with a buoyancy of 320 kg. The ADV pressure cases were clamped to one  
117 side of the strongback fin and the ADV sensor head was positioned 10 cm in front of the fin's  
118 leading edge (Figure 2). The leading edge of the fin is fastened inline with the mooring line. This  
119 configuration was designed to work like a weather vane, such that the drag on the fin held the ADV  
120 head upstream of the mooring components. This work utilizes data from two TTM deployments.

### 121 1) JUNE 2012 TTM DEPLOYMENT

122 The first TTM deployment was in June 2012 from 17:30 on the 12th until 14:30 on the 14th  
123 (local; i.e., Pacific Daylight Time). Two Nortek ADVs were clamped to either side of the fin so that  
124 the axis of their cylindrical pressure cases were parallel with the leading edge of the strongback.

125 The ADV heads were spaced 0.5 m apart vertically along the fin. Only one of these ADVs was  
126 equipped with an integrated IMU. This TTM also had an upward-looking acoustic Doppler profiler  
127 mounted on the mooring anchor.

128 Periods of time during which this mooring interfered with a beam of the Doppler profiler were  
129 identified by inspecting the profiler's acoustic amplitude signal. Periods during which one beam  
130 of the profiler had  $> 5\%$  higher acoustic amplitude than the other beams were flagged as "contam-  
131 inated" and excluded from averaging. Five-minute averages in which more than 50% of the data  
132 were contaminated in this way were masked as invalid.

## 133 2) JUNE 2014 TTM DEPLOYMENT

134 The second TTM deployment was in 2014 from 06:00 on June 17 to 05:00 on June 19 (local  
135 time). Two Nortek ADV-IMUs were mounted on this TTM, with their heads spaced 0.5 m apart  
136 along the fin. In this case, the pressure cases and ADV heads were inclined at an angle of  $18^\circ$  to  
137 the leading edge of the fin to account for mooring blowdown during strong currents (Figure 3).  
138 This change was made to reduce vibrational motion observed during the June 2012 deployment  
139 that was believed to be associated with the orientation of the pressure cases.

### 140 *b. The StableMoor platform*

141 The second deployment platform was a cylindrical, StableMoor, syntactic foam buoy (manufac-  
142 turer: Deep Water Buoyancy) that was anchored to a clump weight that weighed 2,700 lbs (Figure  
143 4). The buoy is 3.5 m long and 0.45 m in diameter with a tail ring that is 0.76 m in diameter. The  
144 StableMoor buoy weighs 295 kg in air, and has a buoyancy of 185 kg in water.

145 The StableMoor buoy was deployed with an ADV-IMU mounted at its nose from 11:21 on May  
146 12 to 11:53 on May 13, 2015 (local time). The sample volume of the ADV is 10 cm forward of

147 the nose and 20 cm above the center line of the StableMoor buoy (Figure 4). Based on Wyngaard  
148 et al.’s (1985) investigation of a similarly shaped slender body, the velocity measurements should  
149 have flow-distortion effects of less than 10%. This configuration was designed to be the most  
150 stable platform for measuring turbulence from a moving platform. The StableMoor buoy was  
151 equipped with a 1,200-kHz RDI workhorse sentinel acoustic Doppler profiler that was oriented  
152 downward-looking to measure water velocity below the platform in twelve 1-m bins and measure  
153 buoy motion (“bottom tracking”), all at a 1-Hz sample rate.

154 The buoy was ballasted to pitch upward a few degrees in zero-flow to avoid “flying downward.”  
155 In the presence of an oncoming current, the tail fins help to orient it into the flow. The anchor for  
156 this buoy is similar to that of the TTM, including an acoustic release so the mooring and anchor  
157 can be recovered separately.

158 The StableMoor platform has two primary advantages compared to the TTM. First, it is signif-  
159 icantly more massive and hydrodynamically stable than the TTM, which reduces the frequency  
160 of motions of the platform. Second, the StableMoor platform is capable of supporting a bottom-  
161 tracking acoustic Doppler profiler, which provides an independent measure of the platform’s trans-  
162 lational motion. Disadvantages of the StableMoor include: its size, which adds to the challenge of  
163 deployment and recovery, and its cost, which is significantly higher than the TTM system.

### 164 *c. Turbulence Torpedo*

165 The turbulence torpedo is a simple sounding weight with an ADV head mounted forward of the  
166 nose, and the ADV pressure case strapped below. This platform was deployed on May 14, 2015,  
167 for 37 minutes starting at 07:41 local time. This measurement was made from a davit that hung  
168 the system from the side of the ship to a depth of approximately 25 m. The primary logistical



advantages of this platform are its compact size, low cost, and the flexibility to perform spatial transects.

#### *d. Coordinate system and turbulence averaging*

Unless stated otherwise, vector quantities in this work are in a fixed “principal-axes” coordinate system that is aligned with the bidirectional tidal flow: positive  $u$  is in the direction of ebb (310° True), positive  $w$  is vertically upward, and  $v$  is the cross-stream component in a right-handed coordinate system. The full velocity vector,  $\vec{u} = (\tilde{u}, \tilde{v}, \tilde{w})$ , is separated into a mean and turbulent component as  $\vec{u} = \overline{\vec{u}} + \vec{u}$ , where the over-bar denotes a 5-minute average. Turbulence kinetic energy,  $\text{tke} = \overline{u^2} + \overline{v^2} + \overline{w^2}$ , and Reynold’s stresses,  $\overline{uv}$ ,  $\overline{uw}$ ,  $\overline{vw}$ , are computed by averaging over the 5-minute window. Throughout this work, we use  $\bar{U} = (\bar{u}^2 + \bar{v}^2)^{1/2}$  to denote the mean horizontal velocity magnitude.

All spectra,  $S\{x\}(f) = |\mathcal{F}\{x(t)\}|^2$ , and cross spectra,  $C\{x,y\}(f) = \text{real}(\mathcal{F}\{x(t)\}\mathcal{F}\{y(t)\})$ , are computed using NumPy fast Fourier transform routines (van der Walt et al. 2011). Here,  $\mathcal{F}\{x(t)\}$  denotes the fast Fourier transform of a signal  $x(t)$ . Time series, e.g.,  $x(t)$ , are linearly detrended and Hanning windowed prior to computing  $\mathcal{F}\{x\}$  to reduce spectral reddening.

Throughout the remainder of this work, the dependence of  $S$  and  $C$  on  $f$  is implied (e.g.,  $S\{x\}(f)$  is hereafter  $S\{x\}$ ), and for other variables the dependence on  $t$  is implied. Spectra and cross spectra are normalized to preserve variance:  $\int S\{u\}df = \overline{u^2}$ , and  $\int C\{u,v\}df = \overline{uv}$ . The notations  $S\{\vec{u}\} = (S\{u\}, S\{v\}, S\{w\})$ , and  $C\{\vec{u}\} = (C\{u,v\}, C\{u,w\}, C\{v,w\})$  denote the set of spectra and cross spectra for each velocity component and pairs of components, respectively.

Turbulence dissipation rates are computed as:

$$\varepsilon = \frac{1}{\bar{U}} \left( \alpha \left\langle (S\{u\} + S\{v\} + S\{w\}) f^{5/3} \right\rangle_{fis} \right)^{3/2} \quad (1)$$

Where  $\alpha = 0.5$ , and  $\langle \rangle_{f_{IS}}$  denotes an average over the inertial subrange of the velocity spectra and where the signal-to-noise ratio is small (Lumley and Terray 1983; Sreenivasan 1995). Throughout this work, we take this average from 0.3 to 1 Hz for the  $u$  and  $v$  components, and 0.3 to 3 Hz for the  $w$  component.

### 3. Methodology

The essential approach of motion correction is to estimate the time series of velocity on a compliant mooring by obtaining an independent estimate of ADV head motion and removing that motion from the measured signal. Previous works have utilized inertial motion sensors to quantify the motion of multiscale profilers for the purpose of measuring the full spectrum of oceanic shear (Winkel et al. 1996). Nortek’s ADV-IMU measures the linear acceleration,  $\vec{a}$ , rotational motion,  $\vec{\omega}$ , and orientation matrix,  $\mathbf{R}$ , of the ADV pressure case (body) in the Earth reference frame. So long as the ADV head is rigidly connected to the ADV pressure case, it is possible to utilize the IMU motion signals to calculate the motion of the ADV head and remove it from the measured velocity signal. A similar approach has been used to correct sonic anemometer measurements of atmospheric turbulence (e.g., Edson et al. 1998; Miller et al. 2008). The ADV head motion is calculated as the sum of rotational and translational motion:

$$\begin{aligned}\vec{u}_h &= \vec{u}_w + \vec{u}_a + \vec{u}_{low} \\ &= \mathbf{R}^T \cdot \vec{\omega}^*(t) \times \vec{\ell}^* + \int \{\vec{a}(t)\}_{HP(f_a)} dt + \vec{u}_{low}\end{aligned}\tag{2}$$

Here,  $*$  superscripts denote quantities in the ADV’s local coordinate system, and  $\vec{\ell}^*$  is the vector from the IMU to the ADV head.  $\mathbf{R}^T$ —the inverse of the orientation matrix—rotates vectors from the IMU to the Earth reference frame. The notation  $\{\vec{a}\}_{HP(f_a)}$  indicates that the IMU’s accelerometer signal is high-pass filtered (in the Earth’s stationary reference frame) at a chosen filter-frequency,  $f_a$ . This is necessary because accelerometers have low-frequency noise, some-

211 times referred to as bias-drift (Barshan and Durrant-Whyte 1995; Bevly 2004; Gulmammadov  
212 2009).

213 Integrating  $\vec{a}$  to estimate  $\vec{u}_a$  amplifies the bias-drift noise at low frequencies, which dramatically  
214 reduces the signal-to-noise ratio at those time scales (Figure A1). The high-pass filtering reduces  
215 this noise so that it does not contaminate motion correction, but real motion that exists at these  
216 frequencies is still lost in the low signal-to-noise ratio (Egeland 2014; VanZwieten et al. 2015).  
217 This means that low-frequency motion is not well resolved by the IMU, and so there is a residual  
218 low-frequency translational motion,  $\vec{u}_{\text{low}}$ , that needs to be measured independently—or at the very  
219 least considered—when using motion-corrected ADV-IMU data. The  $\vec{\omega}$  and  $\vec{u}_\omega$  estimates do not  
220 have the same issue because there is no integration involved, and because low-frequency bias-drift  
221 in the  $\vec{\omega}$  sensors is stabilized by the IMU’s on-board Kalman filtering (i.e., the accelerometer and  
222 magnetometer signals provide estimates of down and north, respectively, which stabilize orienta-  
223 tion estimates and eliminates bias from rotation estimates).

224 The choice of a high-pass filter for reducing low-frequency accelerometer noise depends on the  
225 flow conditions of the measurement and the platform being used. In particular, filter selection in-  
226 volves a trade-off between filtering out the bias-drift noise while not filtering out measured motion  
227 that is unresolved by an independent measurement of  $\vec{u}_{\text{low}}$ . If an independent measure of low-  
228 frequency motion is available it can be used to increase the accuracy of  $\vec{u}_h$  at low frequency. Note  
229 that, to avoid double counting,  $\vec{u}_{\text{low}}$  should be estimated by applying the complementary low-pass  
230 filter to the independent measurement of low-frequency motion.

231 With this estimate of ADV head motion, it is straightforward to correct the measured velocity,  
232  $\vec{u}_m$ , to estimate the velocity in the Earth’s inertial reference frame:

$$\vec{u}(t) = \vec{u}_m(t) + \vec{u}_h(t). \quad (3)$$

233 Note here that the ‘+’-sign is correct because head motion,  $\vec{u}_h$ , induces a measured velocity in the  
234 opposite direction of the head motion itself ( $\vec{u}_m = \vec{u} - \vec{u}_h$ ).

235 For the TTM and turbulence torpedo, we utilize  $f_a = 0.0333\text{Hz}$  (30-s period) and assume that  
236  $\vec{u}_{\text{low}} = 0$ . For the StableMoor buoy,  $f_a = 0.2\text{Hz}$  (5-s period). The bottom-track velocity was low-  
237 pass filtered at this frequency to provide an estimate of  $\vec{u}_{\text{low}}$ , and  $\vec{a}$  was high-pass filtered at this  
238 frequency. We use 4-pole, bidirectional (zero-phase), Hanning filters for all filtering operations.

239 Additional details on motion correction—including a detailed accounting of the distinct co-  
240 ordinate systems of the IMU, ADV pressure case, and ADV head—can be found in Kilcher  
241 et al. (2016). Open-source Python tools for performing motion correction of ADV-IMU data—  
242 including scripts that write processed data in Matlab and tabulated formats—are available at  
243 <http://lkilcher.github.io/dolfyn/>.

## 244 4. Results

### 245 a. Mean velocity

246 Figure 7 shows a comparison of  $\vec{u}$  measured by an ADV-IMU mounted on a TTM, to an upward-  
247 looking acoustic Doppler profiler mounted on the TTM anchor. This comparison shows excellent  
248 agreement between the ADV and Doppler profiler measurements of mean velocity. The  $\bar{u}$ ,  $\bar{v}$ , and  
249  $\bar{w}$  components have a root-mean-square error of 0.05, 0.13, and 0.03 m/s, respectively. Although  
250 it is important to note that there is some discrepancy between ADP- and ADV-measured velocities  
251 (especially in  $\bar{v}$ , which is most likely due to incomplete motion correction), the agreement between  
252 the magnitude and direction of these independent velocity measurements indicates that moored  
253 ADV-IMUs provide a reliable estimate of velocity in the Earth’s reference frame.

## *b. TTM spectra*

As discussed in detail in Part 1, the mooring motion of the TTM,  $S\{\vec{u}_h\}$ , has a peak at 0.1 to 0.2 Hz from swaying of the mooring that is most likely driven by eddy shedding from the spherical buoy (Figure 8, red lines). There is also higher-frequency broadband motion that is associated with fluttering of the strongback fin around the mooring line. Both of these motions are especially energetic in the  $v$ -component spectra because this is the direction in which the TTM mooring system is most unstable. As is expected from fluid-structure interaction theory, the amplitude of these motions increases with increasing mean velocity (Morison et al. 1950).

The mooring motion contaminates the uncorrected ADV measurements of velocity,  $S\{\vec{u}_m\}$ , whenever the amplitude of the motion is similar to or greater than the amplitude of the turbulence. Fortunately, much of this motion can be removed using the IMU's motion signals as detailed in Section 3. Lacking an independent measurement of turbulence velocity at this site, we interpret the agreement of these spectra with turbulence theory as evidence of the success of the method. In particular, at high frequencies ( $f > 0.3$  Hz) for each mean-flow speed, the spectra decay with a  $f^{-5/3}$  slope and have equal amplitude across the velocity components. These results are consistent with Kolmogorov's (1941) theory of isotropic turbulence, and are consistent with spectral shapes of earlier measurements of turbulence in energetic tidal channels from stationary platforms (Walter et al. 2011; Thomson et al. 2012; McMillan et al. 2016).

For  $|\vec{u}| > 1.0$ , motion correction modifies the  $u$  and  $v$  component spectra at frequencies as high as 3 Hz. This outcome indicates that in order for motion correction to be effective, synchronization between the ADV and IMU needs to be within 1/3 s or better. This suggests that asynchronous approaches to motion correction may be challenging, especially considering that the clock drift of

some instrumentation can be as high as a few seconds per day. By integrating the IMU data into the ADV data stream, the Nortek ADV-IMU achieves a synchronization to within 1e-2 s.

At low frequencies the spectra tend to become roughly constant (especially at higher flow speeds), which is also consistent with previous works. Note that the very low magnitude of  $S\{\vec{u}_h\}$  at low frequencies is partially a result of filtering the IMU's accelerometer signal when calculating  $\vec{u}_a$ . The true low-frequency spectrum of ADV head motion is unknown (indicated using a dashed line below  $f_a$ ). A comparison of  $S\{\vec{u}\}$  measured by the TTM to that measured by the ADP—during the June 2012 deployment—reveals agreement at low frequencies (not shown). This finding suggests that the assumption that  $\vec{u}_{\text{low}} = 0$  at these frequencies and at this site for this platform is justified—even if  $S\{\vec{u}_h\}$  is not as low as indicated in Figure 8.

As successful as motion correction is, some of the motion contamination persists in  $S\{\vec{u}\}$ . This is most notable in  $S\{v\}$  at the highest flow speeds ( $> 2.0$  m/s): a peak at 0.15 Hz is an order of magnitude larger than a spectral fit to the other frequencies would indicate. This persistent motion contamination is evident to a lesser degree in  $S\{u\}$  for  $|u| > 2$  m/s, and in  $S\{v\}$  at lower flow speeds.  $S\{w\}$  appears to have no persistent motion contamination because the amplitude of the motion in this direction is much lower than for the other two components. For these measurements,  $S\{w_h\}$  is so low that  $w$ -component motion correction makes only a minor correction to the spectra.

The amplitude of the persistent motion contamination peaks in  $S\{v\}$  at 0.15 Hz is a factor of 5 to 10 times smaller than the amplitude of the ADV head motion itself. This observation suggests that the Microstrain IMU can be used to effectively correct mooring motion at 0.15 Hz when the amplitude of that motion is less than 5 times the amplitude of the real turbulence spectrum. As a result, we have chosen a value of 3 as a conservative estimate of the motion correction's effectiveness.

299 In addition to the primary benefit of correcting for mooring motion, the IMU measurements  
 300 can also be used to identify and screen out persistent motion contamination. For example, one  
 301 of the most common uses of turbulence spectra is for the calculation of  $\varepsilon$  and  $\text{tke}$ . For these  
 302 purposes, and based on the relative amplitudes of the 0.15-Hz peaks, we assume that persistent  
 303 motion contamination is likely, where  $S\{\vec{u}_h\}/S\{\vec{u}\} > 3$ , and thereby exclude these regions from  
 304 spectral fits.

305 In the present case, for the  $u$  and  $w$  spectra, this criteria only excludes a narrow range of frequen-  
 306 cies at the 0.15-Hz motion peak for some cases. This criteria is more restrictive of the  $v$ -component  
 307 spectra at high frequencies for  $\bar{U} > 1.0$  m/s, but this may be acceptable because the amplitude of  
 308  $S\{v\}$  at these frequencies—i.e., in the isotropic inertial subrange—should be equal to that of  $S\{u\}$   
 309 and  $S\{w\}$  (Kolmogorov 1941).

310 Agreement of the  $v$ -component spectral amplitude with that of  $u$  and  $w$  at frequencies  $> 0.3$  Hz  
 311 indicates that motion correction is effective at those frequencies even when  $S\{\vec{u}_h\}/S\{\vec{u}\} \gtrsim 3$ . This  
 312 outcome suggests that our screening threshold is excessively conservative at those frequencies,  
 313 and that a more precise screening threshold may be frequency dependent. For example, it might  
 314 take into account the  $f^3$  character of the noise in  $S\{\vec{u}_a\}$  (Figure A1). For the purpose of this work,  
 315 the  $S\{\vec{u}_h\}/S\{\vec{u}\} < 3$  threshold for spectral fits is sufficient, and detailed characterization of the  
 316 IMU’s motion- and frequency-dependent noise level is left for future work.

### 317 *c. StableMoor Spectra*

318 The spectra of the StableMoor motion has a broader peak with a maximum amplitude that is ap-  
 319 proximately half the frequency of the TTM spectral peak (Figure 9). The motion of this platform  
 320 also does not have high-frequency “subpeaks” or other high-frequency broadbanded excitation

(Part 1). These characteristics of the motion are most likely due to the more massive and hydrodynamically streamlined properties of the platform.

Like the TTM, the motion-corrected spectra from the StableMoor buoy are consistent with turbulence theory and previous observations. Most importantly, there is an improvement in the quality of the motion-corrected spectra compared to the TTM. In particular, the persistent motion contamination peaks are completely removed. That is, this measurement system provides an accurate estimate of the turbulence spectra at this location from low frequencies to more than 1 Hz—well into the inertial subrange—for all three components of velocity.

Note that this level of accuracy cannot be obtained without the independent estimate of  $\vec{u}_{\text{low}}$ . If we assume that  $\vec{u}_{\text{low}} = 0$ , a similar plot to Figure 9 (not shown) reveals persistent motion-contamination peaks and troughs in the  $u$  and  $v$  spectra regardless of the choice of  $f_a$ . This assumption indicates that the low-frequency motion of the StableMoor buoy is below a threshold in which the IMU’s signal-to-noise ratio is high enough to resolve its motion. In other words, compared to the TTM, the StableMoor platform provides a more accurate measurement of turbulence when it includes an independent measure of  $\vec{u}_{\text{low}}$  (here a bottom-tracking ADCP), but it does no better—and perhaps worse—when it does not.

#### *d. Torpedo spectra*

The  $u$  and  $v$  motion of the turbulence torpedo is broadband and the  $w$  motion has a narrow peak at 0.3 Hz (Figure 10). Because  $\vec{u}_h$  is estimated using  $f_a = 0.0333\text{Hz}$  and assuming  $\vec{u}_{\text{low}} = 0$ , its spectra rolls off quickly below  $f_a$ . Motion correction of the torpedo data appears to effectively remove a motion peak from  $S\{w\}$  at 0.3 Hz, and straightens out  $S\{v\}$  between 0.04 and 0.6 Hz.  $S\{u\}$  is mostly unaffected by motion at these frequencies, because the torpedo motion is smaller than the turbulence in this direction. At frequencies below  $f_a$ ,  $S\{u\}$  and  $S\{v\}$  increase



dramatically. This increase suggests that unresolved, low-frequency motion of the torpedo is contaminating the velocity measurements at these frequencies. It may be possible to correct for some of this contamination using a measurement of the ship's motion as a proxy for the torpedo's low-frequency motion, but this has not been done. Still, above  $f_a$ , the torpedo appears to provide a reliable estimate of spectral amplitude in the inertial subrange and can therefore be used to estimate  $\epsilon$ . Considering the simplicity of the platform, it may be a useful option for quantifying this essential turbulence quantity in a variety of scenarios. Further, if a GPS is positioned above it, it may be capable of providing even more.

#### e. *Cross Spectra*

Inspection of cross spectra from TTM measurements demonstrates that motion correction can reduce motion contamination to produce reliable estimates of velocity cross spectra (Figure 11). At low flow speeds (left column), cross spectra between components of  $\vec{u}_h$  (i.e., between components of head motion, red) are small compared to correlated velocities. As the velocity magnitude increases (center and right columns), the swaying motion of the TTM at 0.15 Hz appears as a peak in the amplitude of the cross spectra of  $\vec{u}_h$  (red) and  $\vec{u}_m$  (black) for all three components of cross spectra (rows). Fortunately, motion correction reduces the amplitude of this peak dramatically so that  $C\{\vec{u}\}$  (blue) is small at 0.15 Hz compared to lower frequencies. Furthermore, the fact that the standard deviation of  $C\{\vec{u}\}$  is also relatively small at 0.15 Hz suggests that motion correction is effective for each spectral window, not just in their mean.

These results indicate that motion-corrected TTM velocity measurements can be used to obtain reliable estimates of turbulence Reynold's stresses, which are the integral of the cross spectra. Without motion correction, Reynold's stress estimates would be contaminated by the large peaks in the cross spectra that are caused by the swaying and fluttering motion of the TTM vane.

367 A similar investigation of StableMoor cross spectra (not shown) indicates that cross-spectral  
368 motion contamination is at a much lower amplitude than for the TTM. The low-frequency ( $< 0.3$   
369 Hz) “swimming” motion of that platform produces a minimal cross-spectral signal, and the relative  
370 large mass of the platform minimizes the kinds of higher-frequency swaying and fluttering that  
371 creates large values of cross-spectral head motion. Thus, the StableMoor platform also produces  
372 reliable estimates of Reynold’s stresses, which are presumed to be improved by motion correction.

## 373 5. Discussion

374 The previous section presented a comparison of  $\vec{u}$  measured by a TTM-mounted ADV to mea-  
375 surements from a co-located ADP. This comparison demonstrated that the IMU provides a reliable  
376 estimate of the ADV’s orientation and that this can be utilized to estimate mean velocity in the  
377 Earth’s reference frame. Turbulence velocity estimates from the same ADP are also in agree-  
378 ment with low-frequency TTM turbulence estimates (not shown), but the ADP does not resolve  
379 turbulence at the scales where motion contamination is strongest (0.1 to 1.0 Hz).

380 Ideally, moored motion-corrected turbulence velocity measurements would be validated against  
381 simultaneous independent validated measurements of turbulence velocity at the same scales and  
382 exact time and location. Accomplishing this, however, involves significant technical challenges  
383 that are not easily overcome—most notably the difficulty of measuring turbulence at the same point  
384 as the moving ADV. A slightly less ideal but much more realistic confirmation of the methodology  
385 might involve comparing the statistics of moored turbulence measurements to those from a nearby  
386 fixed platform, or a fixed platform placed at the same location at a different time (e.g., the “TTT”  
387 platform described in Thomson et al. 2012). Unfortunately, to our knowledge, these measurements  
388 have not yet been made.

389 Lacking a relevant, fixed, independent turbulence measurement to compare to it is instructive  
 390 to demonstrate the degree to which the moored measurements are consistent with turbulence  
 391 theory and other turbulence measurements in similar flow environments. The previous section  
 392 showed that the shape of the turbulence velocity spectra from moored ADVs is consistent with  
 393 Kolmogorov’s theory of locally isotropic turbulence, which has been observed consistently in tur-  
 394 bulence measurements for decades (Kolmogorov 1941; Grant et al. 1962; McMillan et al. 2016).  
 395 In particular, we observed an isotropic subrange—an  $f^{-5/3}$  spectral slope and equal amplitude  
 396 spectra between components—that is driven by anisotropic turbulence at longer timescales (Fig-  
 397 ures 8, 9, 10). This finding is interpreted as the first indication that the measurement systems  
 398 presented are capable of accurately resolving turbulence. The degree to which uncorrected spec-  
 399 tra were corrected toward this theoretical and observationally confirmed shape is interpreted as a  
 400 measure of the improvement of the spectral estimates by motion correction.

401 Figure 12 presents a time series of the mean velocity (A) and several turbulence statistics that  
 402 were measured during the June 2014 TTM deployment. This figure shows the evolution of the flow  
 403 through Admiralty Inlet during 1.5 tidal cycles. The tke (B), Reynold’s stresses (C), dissipation,  
 404 and one component of turbulence production (D) grow and strengthen with ebb or flood then  
 405 subside during slack tide. This component of turbulence production is:

$$P_{uz} = \frac{\partial \bar{u}}{\partial z} \overline{uw} \quad . \quad (4)$$

406 Where  $\partial \bar{u} / \partial z$  is computed from the two ADVs on the TTM. The highest values of  $\varepsilon$  and  $P_{uz}$  occur  
 407 at the peak of the ebb or flood, which is in agreement with other measurements in tidal channels.  
 408 The agreement of the magnitude of  $P_{uz}$  with  $\varepsilon$  at those times suggests a local production-dissipation  
 409 balance that is often observed in tidally forced channels (Trowbridge et al. 1999; Stacey et al.

1999b; McMillan et al. 2016). At other times, the value of  $P_{uz}$  is insufficient to balance  $\varepsilon$  or is negative.

Inspection of the negative  $P_{uz}$  values reveals that most of them are caused by a reversed sign of  $\overline{uw}$  rather than a reversed sign of  $\partial u / \partial z$  (i.e., when compared to the sign of  $u$ ). This finding suggests that uncertainty in  $\overline{uw}$  may be contributing to discrepancies between  $P_{uz}$  and  $\varepsilon$ . Furthermore, considering the complex nature of the shoreline near this site (i.e., the headland), it is not surprising that  $P_{uz}$  does not balance  $\varepsilon$  perfectly. Other terms of the tke equation are likely to be important, such as other components of production, advection terms, or turbulent transport terms. The fact that these two terms are in near balance as often as they are is a strong indication that bottom boundary layer physics are important to the dynamics at this site.

Figure 13 compares individual values of  $P_{uz}$  with  $\varepsilon$  directly. Given the assumptions implicit in this comparison and the discussion above, the agreement between  $P_{uz}$  and  $\varepsilon$  is an encouraging result that suggests the turbulent boundary reaches the depth of these measurements (10 m) during the highest flow speeds. This result is further supported by a comparison of  $\bar{U}$  with  $\varepsilon$  (Figure 14). Here we see a  $\varepsilon \propto \bar{U}^3$  dependence that is again suggestive of bottom boundary layer physics (Trowbridge 1992; Nash et al. 2009). At lower flow speeds,  $\varepsilon$  deviates from this relationship, which suggests that the boundary layer is no longer the dominant physical process at the depth of these measurements.

## 6. Conclusion

This work presents a methodology for measuring turbulence from moored ADV-IMUs and details an approach for removing the IMU-measured mooring motion from the ADV's velocity measurements. The IMU integrated into the Nortek Vector ADV has been configured to provide estimates of the ADV's orientation and motion at every time step of the ADV's sampling. The tight

433 integration of the IMU and ADV data streams provides a data set that can be used to correct ve-  
434 locity measurements for mooring motion and rotate those measurements into the Earth’s reference  
435 frame.

436 Comparison of spectra of ADV head motion,  $S\{\vec{u}_h\}$ , to that of motion-corrected,  $S\{\vec{u}\}$ , and  
437 uncorrected spectra,  $S\{\vec{u}_m\}$ , reveals that motion correction improves spectral estimates of moored  
438 ADV measurements. In particular, we found that motion-corrected spectra have spectral shapes  
439 that are similar to previous measurements of tidal-channel turbulence and have a  $f^{-5/3}$  spectral  
440 slope at high frequencies. This finding suggests that the motion-corrected spectra resolve the  
441 inertial subrange predicted by Kolmogorov’s theory of locally isotropic turbulence.

442 Motion correction reduces motion contamination for all platforms we presented but it does not  
443 necessarily remove it completely. This outcome seems to depend on the relative amplitude of  
444 platform motion compared to the underlying turbulence being measured. The most notable ex-  
445 ample of this is from the TTM, which has a large “swaying” peak at 0.1 Hz. Where this peak  
446 is very large—especially in the  $v$  component—it is not reduced to a level that is consistent with  
447 earlier measurements of tidal-channel turbulence—i.e., there is no smooth roll-off between the  
448 low-frequency energy-containing scales and the  $f^{-5/3}$  inertial subrange.

449 This inconsistency indicates that turbulence measurements from moored, motion-corrected IMU  
450 ADVs must be interpreted with care. An inspection of spectra presented here suggests that exclud-  
451 ing spectral regions where  $S\{\vec{u}_h\}/S\{\vec{u}\} > 3$  removes persistent-motion contamination peaks while  
452 still preserving spectral regions where motion correction is effective. Using this criteria, it is then  
453 possible to produce spectral fits that exclude persistent-motion contamination, and provide reliable  
454 estimates of turbulence quantities of interest (e.g.,  $\varepsilon$  and  $\text{tke}$ ).

455 We’ve also shown that motion correction reduces motion contamination in cross spectra. This  
456 finding is important because it suggests that moored IMU-ADV measurements may be used to

457 produce reliable estimates of Reynolds stresses. We utilized these stress estimates and vertical  
458 shear estimates, both from the TTM, to estimate  $P_{uz}$ .

459 Finally, we have shown that  $\varepsilon$  estimates based on motion-corrected spectra scale with the  $U^3$ , and  
460 balance  $P_{uz}$  estimates during ebb and flood. Together, these results indicate that bottom boundary  
461 layer physics are a dominant process at this site, and that the boundary layer reaches the height  
462 of the IMU ADVs (10 m) during ebb and flood. The degree of agreement between  $P_{uz}$  and  $\varepsilon$  also  
463 serves as an indicator of the self-consistency of moored IMU-ADV turbulence measurements.

464 *Acknowledgments.* Many thanks to Joe Talbert, Alex DeKlerk, Captain Andy Reay-Ellers, Jen-  
465 nifer Rinker, Maricarmen Guerra, and Eric Nelson in assisting with data collection. The authors  
466 are also grateful to James VanZwieten, Matthew Egeland and Marshall Richmond for discussion  
467 on the details of this work.

468 This work was supported by the U.S. Department of Energy under Contract No. DE-AC36-  
469 08GO28308 with the National Renewable Energy Laboratory. Funding for the work was provided  
470 by the DOE Office of Energy Efficiency and Renewable Energy, Wind and Water Power Technolo-  
471 gies Office.

472 The U.S. Government retains and the publisher, by accepting the article for publication, ac-  
473 knowledges that the U.S. Government retains a nonexclusive, paid-up, irrevocable, worldwide  
474 license to publish or reproduce the published form of this work, or allow others to do so, for U.S.  
475 Government purposes.

## 477 **A1. Comparing StableMoor $\vec{u}_{\text{low}}$ to IMU $\vec{u}_{\text{h}}$**

478 To better understand the IMU’s signal-to-noise ratio, we compare the motion of the StableMoor  
 479 buoy from the ADP bottom track measurements,  $\vec{u}_{\text{BT}}$ , to the IMU’s estimates of ADP motion.  
 480 To do this, we compute the IMU’s estimate of ADP motion using equation (2), and replacing  $\ell^*$   
 481 with the vector that points from the IMU to the ADP head. We then linearly interpolate the ADP  
 482 measurements of  $\vec{u}_{\text{BT}}$  onto the times of the ADV-IMU measurements.

483 The coherence between these two signals is high and statistically significant over 1.5 decades—  
 484 from 0.03 to 0.8 Hz (Priestley 1981). The  $v$  component has the highest coherence, 98%, because  
 485 this is the direction that has the most motion (i.e., these estimates have a higher signal-to-noise  
 486 ratio). The  $u$  and  $w$  components have a slightly lower coherence, 80% and 65%, respectively.

487 On the low-frequency side, our interpretation is that the signal-to-noise ratio of the IMU in-  
 488 creases dramatically below 0.03 Hz, resulting in low coherence. On the high-frequency side,  
 489 Doppler noise in the ADP measurements contaminates its estimates of motion, causing the de-  
 490 crease in coherence at 0.8 Hz. A comparison of the phase between these signals shows that there  
 491 is no lag between the measurements (not shown).

492 These results help to inform the selection of zero-lag filters used to estimate  $\vec{u}_{\text{low}}$  from  $\vec{u}_{\text{BT}}$ .  
 493 In particular, by selecting 0.2 Hz, we target the middle of the coherence peak between the two  
 494 measurements. Furthermore, the rapid decrease in coherence below 0.03 Hz provides an objective  
 495 measurement of the frequency at which IMU measured velocity becomes unreliable in the flow  
 496 conditions we observed.

## References

- Afgan, I., J. McNaughton, S. Rolfo, D. Apsley, T. Stallard, and P. Stansby, 2013: Turbulent flow and loading on a tidal stream turbine by les and rans. *International Journal of Heat and Fluid Flow*, **43**, 96–108.
- Alexander, S. R., and P. E. Hamlington, 2015: Analysis of turbulent bending moments in tidal current boundary layers. *Journal of Renewable and Sustainable Energy*, **7** (6), 063 118.
- Alford, M. H., 2010: Sustained, full-water-column observations of internal waves and mixing near mendocino escarpment. *Journal of Physical Oceanography*, **40** (12), 2643–2660, doi:10.1175/2010JPO4502.1.
- Axford, D., 1968: On the accuracy of wind measurements using an inertial platform in an aircraft, and an example of a measurement of the vertical mesostructure of the atmosphere. *Journal of Applied Meteorology*, **7** (4), 645–666.
- Bachmann, E. R., X. Yun, D. McKinney, R. B. McGhee, and M. J. Zyda, 2003: Design and implementation of MARG sensors for 3-DOF orientation measurement of rigid bodies. *International Conference on Robotics & Automation*, Taipei, Taiwan.
- Barshan, B., and H. F. Durrant-Whyte, 1995: Inertial navigation systems for mobile robots. *IEEE Transactions on Robotics and Automation*, **11** (3), 328–342.
- Bevly, D. M., 2004: Global positioning system (gps): A low-cost velocity sensor for correcting inertial sensor errors on ground vehicles. *Journal of dynamic systems, measurement, and control*, **126** (2), 255–264.



517 Cartwright, G. M., C. T. Friedrichs, P. J. Dickhudt, T. Gass, and F. H. Farmer, 2009: Using the  
518 acoustic doppler velocimeter (adv) in the mudbed real-time observing system. *Marine Technol-  
519 ogy for Our Future: Global and Local Challenges*.

520 Doherty, K., D. Frye, S. Liberatore, and J. Toole, 1999: A moored profiling instrument\*. *Journal  
521 of Atmospheric and Oceanic Technology*, **16 (11)**, 1816–1829.

522 Edson, J. B., A. A. Hinton, K. E. Prada, J. E. Hare, and C. W. Fairall, 1998: Direct covariance  
523 flux estimates from mobile platforms at sea\*. *Journal of Atmospheric and Oceanic Technology*,  
524 **15 (2)**, 547–562, doi:10.1175/1520-0426(1998)015<0547:DCFEFM>2.0.CO;2.

525 Egeland, M. N., 2014: Spectral evaluation of motion compensated ADV systems for ocean turbu-  
526 lence measurements. Ph.D. thesis, Florida Atlantic University.

527 Fer, I., and M. B. Paskyabi, 2014: Autonomous ocean turbulence measurements using shear probes  
528 on a moored instrument. *Journal of Atmospheric and Oceanic Technology*, **31 (2)**, 474–490, doi:  
529 10.1175/JTECH-D-13-00096.1.

530 Finlayson, D., 2005: Combined bathymetry and topography of the Puget Lowlands, Washington  
531 state. URL <http://www.ocean.washington.edu/data/pugetsound/>.

532 Geyer, R. W., M. E. Scully, and D. K. Ralston, 2008: Quantifying vertical mixing in estuaries.  
533 *Environmental Fluid Mechanics*, **8**, 495–509, doi:10.1007/s10652-008-9107-2.

534 Goodman, L., E. R. Levine, and R. G. Lueck, 2006: On measuring the terms of the turbulent  
535 kinetic energy budget from an auv. *Journal of Atmospheric and Oceanic Technology*, **23 (7)**,  
536 977–990, doi:10.1175/JTECH1889.1.

537 Grant, H. L., R. W. Stewart, and A. Moilliet, 1962: Turbulence spectra from a tidal channel.  
538 *Journal of Fluid Mechanics*, **12**, 241–263.

539 Gulmammadov, F., 2009: Analysis, modeling and compensation of bias drift in mems inertial  
540 sensors. *Recent Advances in Space Technologies, 2009. RAST'09. 4th International Conference*  
541 *on*, IEEE, 591–596.

542 Gunawan, B., V. S. Neary, and J. Colby, 2014: Tidal energy site resource assessment in the East  
543 River tidal strait, near Roosevelt Island, New York, NY (USA). *Renewable Energy*, **71**, 509–  
544 517, doi:10.1016/j.renene.2014.06.002.

545 Hand, M. M., N. D. Kelley, and M. J. Balas, 2003: Identification of wind turbine response to  
546 turbulent inflow structures. Tech. Rep. NREL/CP-500-33465, National Renewable Energy Lab-  
547 oratory.

548 Harding, S., L. Kilcher, and J. Thomson, 2017: Turbulence measurements from compliant moor-  
549 ings - part 1: Motion characterization, in review.

550 Kelley, N. D., B. J. Jonkman, G. N. Scott, J. T. Bialasiewicz, and L. S. Redmond, 2005: The impact  
551 of coherent turbulence on wind turbine aeroelastic response and its simulation. *WindPower*,  
552 Denver, Colorado, NREL/CP-500-38074, may 15-18.

553 Kilcher, L., J. Thomson, J. Talbert, and A. DeKlerk, 2016: Measuring turbulence from moored  
554 acoustic Doppler velocimeters: A manual to quantifying inflow at tidal energy sites. 9 62979,  
555 National Renewable Energy Laboratory. URL [www.nrel.gov/docs/fy16osti/62979.pdf](http://www.nrel.gov/docs/fy16osti/62979.pdf).

556 Kim, S. C., C. T. Friedrichs, J. P.-Y. Maa, and L. D. Wright, 2000: Estimating bottom stress in  
557 tidal boundary layer from acoustic doppler velocimeter data. *Journal of Hydraulic Engineering*,  
558 399–406.

559 Kolmogorov, A. N., 1941: Dissipation of energy in the locally isotropic turbulence. *Dokl. Akad.*  
560 *Nauk SSSR*, **32** (1), 16–18, URL <http://www.jstor.org/stable/51981>.

561 Kraus, C., A. Lohrmann, and R. Cabrera, 1994: A new acoustic meter for measuring 3d laboratory  
562 flows. *Journal of Hydraulic Engineering*, **120**, 406–412.

563 Lohrmann, A., R. Cabrera, G. Gelfenbaum, and J. Haines, 1995: Direct measurements of reynolds  
564 stress with an acoustic doppler velocimeter. *Current Measurement, 1995., Proceedings of the*  
565 *IEEE Fifth Working Conference on*, 205–210, doi:10.1109/CCM.1995.516175.

566 Lorke, A., 2007: Boundary mixing in the thermocline of a large lake. *Journal of Geophysical*  
567 *Research: Oceans*, **112 (C9)**, n/a–n/a, doi:10.1029/2006JC004008, c09019.

568 Lueck, R. G., and D. Huang, 1999: Dissipation measurement with a moored instrument in a swift  
569 tidal channel. *Journal of atmospheric and oceanic technology*, **16**, 1499–1505.

570 Lumley, J., and E. Terray, 1983: Kinematics of turbulence convected by a random wave field.  
571 *Journal of Physical Oceanography*, **13 (11)**, 2000–2007.

572 Marins, J. L., X. Yun, E. R. Bachmann, R. B. McGhee, and M. J. Zyda, 2001: An extended Kalman  
573 filter for quaternion-based orientation estimation using MARG sensors. *Internation cconference*  
574 *on intelligent robots and systems*.

575 McCaffrey, K., B. Fox-Kemper, P. E. Hamlington, and J. Thomson, 2015: Characterization of  
576 turbulence anisotropy, coherence, and intermittency at a prospective tidal energy site: Observa-  
577 tional data analysis. *Renewable Energy*, **76**, 441–453.

578 McMillan, J. M., A. E. Hay, R. G. Lueck, and F. Wolk, 2016: Rates of dissipation of turbulent  
579 kinetic energy in a high reynolds number tidal channel. *Journal of Atmospheric and Oceanic*  
580 *Technology*, **33 (4)**, 817–837, doi:10.1175/JTECH-D-15-0167.1.

581 MicroStrain, I., 2010: Technical note: Coning and sculling. Tech. Rep. I0019, MicroStrain. URL  
582 [http://files.microstrain.com/TN-I0019\\_3DM-GX3-25\\_\\_Coning\\_And\\_Sculling.pdf](http://files.microstrain.com/TN-I0019_3DM-GX3-25__Coning_And_Sculling.pdf).

583 MicroStrain, I., 2012: *3DM-GX3-15,-25 MIP Data Communications Protocol*. URL [http:](http://files.microstrain.com/3DM-GX3-15-25-MIP-Data-Communications-Protocol.pdf)  
584 [//files.microstrain.com/3DM-GX3-15-25-MIP-Data-Communications-Protocol.pdf](http://files.microstrain.com/3DM-GX3-15-25-MIP-Data-Communications-Protocol.pdf), retrieved  
585 January 2014.

586 Miller, S. D., T. S. Hristov, J. B. Edson, and C. A. Friehe, 2008: Platform motion effects on  
587 measurements of turbulence and air-sea exchange over the open ocean. *Journal of Atmospheric*  
588 *and Oceanic Technology*, **25 (9)**, 1683–1694, doi:10.1175/2008JTECHO547.1.

589 Morison, J. R., J. W. Johnson, and S. A. Schaaf, 1950: The force exerted by surface waves on  
590 piles. *Journal of Petroleum Technology*, **2 (05)**, 149–154.

591 Moum, J., and J. Nash, 2009: Mixing measurements on an equatorial ocean mooring. *Journal of*  
592 *Atmospheric and Oceanic Technology*, **26 (2)**, 317–336.

593 Mücke, T., D. Kleinhans, and J. Peinke, 2011: Atmospheric turbulence and its influence on the  
594 alternating loads on wind turbines. *Wind Energy*, **14**, 301–316.

595 Nash, J. D., L. F. Kilcher, and J. N. Moum, 2009: Structure and composition of a strongly  
596 stratified, tidally pulsed river plume. *Journal of Geophysical Research*, **114**, C00B12, doi:  
597 10.1029/2008JC005036.

598 Nash, J. D., E. Kunze, J. M. Toole, and R. W. Schmitt, 2004: Internal tide reflection and turbulent  
599 mixing on the continental slope. *Journal of Physical Oceanography*, **34 (5)**, 1117–1134, doi:  
600 10.1175/1520-0485(2004)034<1117:ITRATM>2.0.CO;2.

601 Nortek, 2005: *Vector Current Meter User Manual*. Vangkroken 2, NO-1351 RUD, Norway, h ed.

602 Paskyabi, M. B., and I. Fer, 2013: Turbulence measurements in shallow water from a subsurface  
603 moored moving platform. *Energy Procedia*, **35**, 307 – 316, doi:10.1016/j.egypro.2013.07.183.

Polagye, B., and J. Thomson, 2013: Tidal energy resource characterization: methodology and field study in admiralty inlet, Puget Sound, WA (USA). *Proceedings of the Institution of Mechanical Engineers, Part A: Journal of Power and Energy*, **227** (3), 352–367.

Priestley, M., 1981: *Spectral Analysis and Time Series*. Academic Press, London.

Rippeth, T. P., E. Williams, and J. H. Simpson, 2002: Reynolds stress and turbulent energy production in a tidal channel. *Journal of Physical Oceanography*, **32**, 1242–1251, doi:10.1175/1520-0485(2002)032\$(<1242:RSATEP\$>\$2.0.CO;2.

Sreenivasan, K. R., 1995: On the universality of the Kolmogorov constant. *Physics of Fluids*, **7**, 2778–2784.

Stacey, M. T., S. G. Monismith, and J. R. Burau, 1999a: Measurements of reynolds stress profiles in unstratified tidal flow. *J. Geophys. Res.*, **104** (C5), 10 933–10 949, doi:10.1029/1998JC900095.

Stacey, M. T., S. G. Monismith, and J. R. Burau, 1999b: Observations of turbulence in a partially stratified estuary. *Journal of Physical Oceanography*, **29**, 1950–1970.

Thomson, J., B. Polagye, V. Durgesh, and M. Richmond, 2012: Measurements of turbulence at two tidal energy sites in Puget Sound, WA. *Journal of Oceanic Engineering*, **37** (3), 363–374, doi:10.1109/JOE.2012.2191656.

Trowbridge, J. H., 1992: A simple description of the deepening and structure of a stably stratified flow driven by a surface stress. *Journal of Geophysical Research*, **97**, 15 529–15 543.

Trowbridge, J. H., W. R. Geyer, M. M. Bowen, and A. J. I. Williams, 1999: Near-bottom turbulence measurements in a partially mixed estuary: turbulent energy balance, velocity structure and along-channel momentum balance. *Journal of Physical Oceanography*, **29**, 3056–3072.

626 van der Walt, S., S. C. Colbert, and G. Varoquaux, 2011: The numpy array: A structure for efficient  
627 numerical computation. *Computing in Science & Engineering*, **13**, 22–30, doi:10.1109/MCSE.  
628 2011.37.

629 VanZwieten, J. H., M. N. Egeland, K. D. von Ellenrieder, J. W. Lovenbury, and L. Kilcher, 2015:  
630 Experimental evaluation of motion compensated adv measurements for in-stream hydrokinetic  
631 applications. *Current, Waves and Turbulence Measurement (CWTM), 2015 IEEE/OES Eleventh*,  
632 1–8, doi:10.1109/CWTM.2015.7098119.

633 Voulgaris, G., and J. H. Trowbridge, 1998: Evaluation of the acoustic doppler velocimeter (adv)  
634 for turbulence measurements. *Journal of Atmospheric and Oceanic technology*, **15**, 272–289.

635 Walter, R. K., N. J. Nidzieko, and S. G. Monismith, 2011: Similarity scaling of turbulence spectra  
636 and cospectra in a shallow tidal flow. *Journal of Geophysical Research: Oceans*, **116 (C10)**.

637 Wiles, P. J., T. P. Rippeth, J. H. Simpson, and P. J. Hendricks, 2006: A novel technique for  
638 measuring the rate of turbulent dissipation in the marine environment. *Geophysical Research*  
639 *Letters*, **33**, 21 608.

640 Winkel, D., M. Gregg, and T. Sanford, 1996: Resolving oceanic shear and velocity with the multi-  
641 scale profiler. *Journal of Atmospheric and Oceanic Technology*, **13 (5)**, 1046–1072.

642 Wyngaard, J. C., L. Rockwell, and C. A. Friehe, 1985: Errors in the measurement of turbulence  
643 upstream of an axisymmetric body. *Journal of Atmospheric and Oceanic Technology*, **2 (4)**,  
644 605–614.

645 Zhang, Y., K. Streitlien, J. G. Bellingham, and A. B. Baggeroer, 2001: Acoustic doppler ve-  
646 locimeter flow measurement from an autonomous underwater vehicle with applications to deep

647 ocean convection. *Journal of Atmospheric and Oceanic Technology*, **18 (12)**, 2038–2051, doi:  
648 10.1175/1520-0426(2001)018<2038:ADVFMF>2.0.CO;2.

## LIST OF FIGURES

|     |                        |   |
|-----|------------------------|---|
| 649 | <b>LIST OF FIGURES</b> |   |
| 650 | <b>Fig. 1.</b>         | Bathymetry of Admiralty Inlet near Port Townsend, Washington, U.S.A. (Finlayson 2005). The red dot indicates the location of all measurements. The positive $u$ direction is the direction of ebb flow (thick arrow originating from red dot), and positive $v$ is away from Admiralty Head (smaller arrow). . . . . 34   |
| 651 |                        |   |
| 652 |                        |   |
| 653 |                        |   |
| 654 | <b>Fig. 2.</b>         | Schematic diagram of the TTM; not to scale. . . . . 35  |
| 655 | <b>Fig. 3.</b>         | TTM components on the deck of the R/V Jack Robertson. The TTM includes two ADVs, with pressure cases mounted on opposite sides of the fin. The anchor stack includes a pop-up buoy for retrieval. The green arrow indicates the vector from the IMU to the ADV head (face of the transmit transducer). . . . . 36   |
| 656 |                        |   |
| 657 |                        |   |
| 658 |                        |   |
| 659 | <b>Fig. 4.</b>         | Top: Alex DeKlerk checks to ensure that the StableMoor buoy is properly fastened to its anchor; the RDI workhorse ADCP can be seen in the rear instrument bay. A bridle is draped across the top of the buoy for deployment and recovery, and a small marker buoy fastened to the tail is useful during recovery. Bottom: a close-up of the StableMoor with the ADV head and the top of its pressure case. The green arrow indicates the vector from the IMU to the ADV head. . . . . 37  |
| 660 |                        |   |
| 661 |                        |   |
| 662 |                        |   |
| 663 |                        |   |
| 664 |                        |   |
| 665 | <b>Fig. 5.</b>         | The turbulence platform showing details of the ADV head and pressure case configuration. The green arrow indicates the vector from the IMU to the ADV head. The head cable was taped out of the way beneath the sounding weight tail fins shortly after taking this photo. . . . 38   |
| 666 |                        |   |
| 667 |                        |   |
| 668 | <b>Fig. 6.</b>         | Spectra of $\vec{u}_\omega$ (yellow) and $\vec{u}_a$ signals from the Microstrain IMU sitting on a motionless table. The $\vec{u}_a$ signals are unfiltered (black), and high-pass filtered at 30 s (magenta), 10 s (blue), 5 s (green). Vertical dotted lines indicate the filter frequency. The black horizontal dotted line indicates the noise level of a Nortek Vector ADV configured to measure $\pm 4\text{m/s}$ . The shaded region indicates the range of spectra presented herein ( $0.002 < \text{tke} < 0.03 \text{ m}^2/\text{s}^2$ , $1\text{e-}5 < \varepsilon < 5\text{e-}4 \text{ W/kg}$ ). . . . . 39   |
| 669 |                        |   |
| 670 |                        |   |
| 671 |                        |   |
| 672 |                        |   |
| 673 |                        |   |
| 674 | <b>Fig. 7.</b>         | Time series of tidal velocity at Admiralty Head from TTM measurements (black), and an acoustic Doppler profiler (red). The profiler measurements—taken at the same depth as the ADV on the TTM—were contaminated by acoustic reflection from the strongback fin when it was inline with one of the profiler’s beams. Note that the vertical scale on the three axes vary by more than an order of magnitude; the small ticks in A and B are equivalent to the ticks in C. . . . . 40  |
| 675 |                        |   |
| 676 |                        |   |
| 677 |                        |   |
| 678 |                        |   |
| 679 |                        |   |
| 680 | <b>Fig. 8.</b>         | Turbulence spectra from the June 2014 TTM deployment. Each column is for a range of streamwise velocity magnitudes (indicated at top). The rows are for each component of velocity (indicated to the lower right of the right column). The uncorrected spectra are in black and the corrected spectra are blue, and the spectra of ADV head motion, $\vec{u}_h$ , is red (also indicated in the legend). The vertical red dotted line indicates the filter frequency applied to the IMU accelerometers when estimating $\vec{u}_h$ ; below this frequency $S\{\vec{u}_h\}$ is plotted as a dashed line. Diagonal black dotted lines indicate a $f^{-5/3}$ slope. The number of spectral ensembles, $N$ , in each column is indicated in the top row. . . . . 41 |
| 681 |                        |   |
| 682 |                        |   |
| 683 |                        |   |
| 684 |                        |   |
| 685 |                        |   |
| 686 |                        |   |
| 687 |                        |   |
| 688 | <b>Fig. 9.</b>         | Turbulence spectra from the StableMoor buoy. The axes layout and annotations are identical to Figure 8, except that $S\{\vec{u}_h\}$ is plotted as a solid line at all frequencies because it is measured at all frequencies. . . . . 42  |
| 689 |                        |   |
| 690 |                        |   |



|     |                 |   |    |
|-----|-----------------|---|----|
| 691 | <b>Fig. 10.</b> | Turbulence spectra from the turbulence torpedo during a 35-minute period when the mean velocity was 1.3 m/s. Annotations and line colors are identical to Figure 8. . . . .   | 43 |
| 692 |                 |   |    |
| 693 | <b>Fig. 11.</b> | The real part of the cross-spectral density between velocity components measured by the TTM. The upper row is the $u$ - $v$ cross-spectral density, the middle row is the $u$ - $w$ cross-spectral density, and the bottom row is the $v$ - $w$ cross-spectral density. The columns are for different ranges of the stream-wise mean velocity magnitude (indicated above the top row). The blue line is the cross spectrum between components of motion-corrected velocity, the red line is the cross spectrum between components of head-motion, and the black line is the cross spectrum between components of uncorrected velocity. The light blue shading indicates one standard deviation of the $C$ for the motion-corrected cross-spectral density. $N$ is the number of spectral ensembles in each column. The number in the lower-right corner of each panel is the motion-corrected Reynold's stress (integral of the blue line) in units of $1\text{e-}4 \text{ m}^2\text{s}^{-2}$ . . . . . | 44 |
| 694 |                 |   |    |
| 695 |                 |   |    |
| 696 |                 |   |    |
| 697 |                 |   |    |
| 698 |                 |   |    |
| 699 |                 |   |    |
| 700 |                 |   |    |
| 701 |                 |   |    |
| 702 |                 |   |    |
| 703 |                 |   |    |
| 704 | <b>Fig. 12.</b> | Time series of mean velocities (A), turbulence energy and its components (B), Reynold's stresses (C), and turbulence dissipation rate (D) measured by the TTM during the June 2014 deployment. Shading indicates periods of ebb ( $\bar{u} > 1.0$ , grey) and flood ( $\bar{u} < -1.0$ , lighter grey). . . . .   | 45 |
| 705 |                 |   |    |
| 706 |                 |   |    |
| 707 |                 |   |    |
| 708 | <b>Fig. 13.</b> | $P_{u\bar{z}}$ vs. $\varepsilon$ during the June 2014 TTM deployment for values of $ u  > 1$ m/s. Values of negative production are indicated as open circles. . . . .  | 46 |
| 709 |                 |   |    |
| 710 | <b>Fig. 14.</b> | A log-log plot of $\varepsilon$ versus $\bar{U}$ for the June 2014 TTM (diamonds) and May 2015 StableMoor (dots) deployments, during ebb (left) and flood (right). Black points are 5-minute averages. Green dots are mean values within speed bins of $0.2 \text{ m s}^{-1}$ width that have at least 10 points (50 minutes of data); their vertical bars are 95% bootstrap confidence intervals. The blue line shows a $U^3$ slope, wherein the proportionality constant (blue box) is calculated by taking the log-space mean of $\varepsilon/U^3$ . . . . .   | 47 |
| 711 |                 |   |    |
| 712 |                 |   |    |
| 713 |                 |   |    |
| 714 |                 |   |    |
| 715 |                 |   |    |
| 716 | <b>Fig. 15.</b> | Coherence between IMU-measured motion of StableMoor buoy and ADP bottom-track velocity for $1.0 < \bar{U} < 1.5$ . The horizontal dotted line indicates the 95% confidence level for the 102 spectral windows in this estimate. . . . .   | 48 |
| 717 |                 |   |    |
| 718 |                 |   |    |

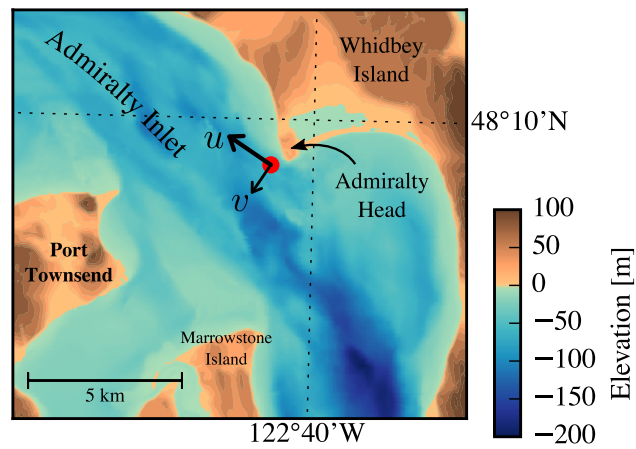


FIG. 1. Bathymetry of Admiralty Inlet near Port Townsend, Washington, U.S.A. (Finlayson 2005). The red dot indicates the location of all measurements. The positive  $u$  direction is the direction of ebb flow (thick arrow originating from red dot), and positive  $v$  is away from Admiralty Head (smaller arrow).

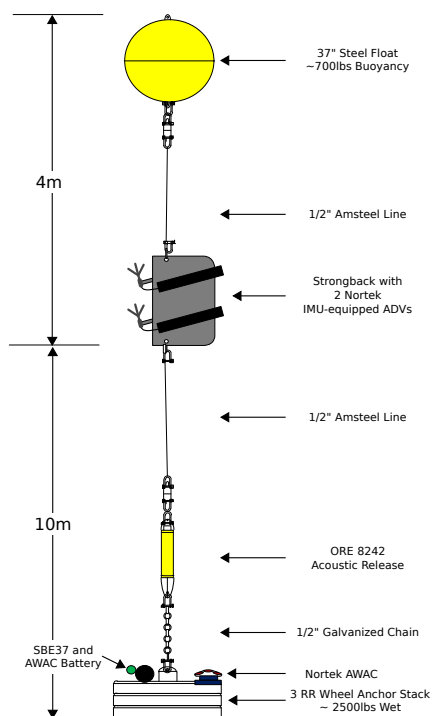


FIG. 2. Schematic diagram of the TTM; not to scale.



722 FIG. 3. TTM components on the deck of the R/V Jack Robertson. The TTM includes two ADVs, with  
 723 pressure cases mounted on opposite sides of the fin. The anchor stack includes a pop-up buoy for retrieval. The  
 724 green arrow indicates the vector from the IMU to the ADV head (face of the transmit transducer).



725 FIG. 4. Top: Alex DeKlerk checks to ensure that the StableMoor buoy is properly fastened to its anchor; the  
 726 RDI workhorse ADCP can be seen in the rear instrument bay. A bridle is draped across the top of the buoy  
 727 for deployment and recovery, and a small marker buoy fastened to the tail is useful during recovery. Bottom: a  
 728 close-up of the StableMoor with the ADV head and the top of its pressure case. The green arrow indicates the  
 729 vector from the IMU to the ADV head.



730 FIG. 5. The turbulence platform showing details of the ADV head and pressure case configuration. The green  
731 arrow indicates the vector from the IMU to the ADV head. The head cable was taped out of the way beneath the  
732 sounding weight tail fins shortly after taking this photo.

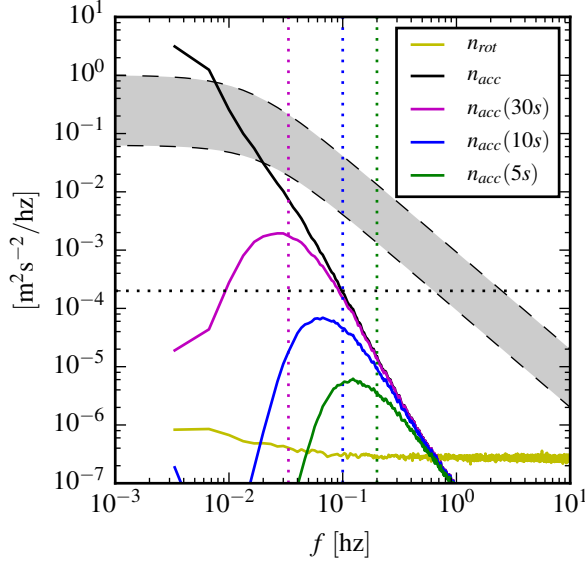
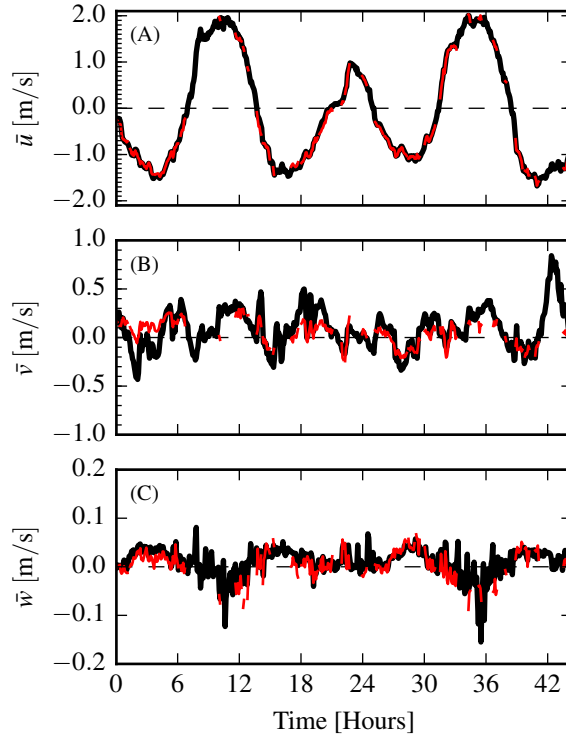


FIG. 6. Spectra of  $\vec{u}_\omega$  (yellow) and  $\vec{u}_a$  signals from the Microstrain IMU sitting on a motionless table. The  $\vec{u}_a$  signals are unfiltered (black), and high-pass filtered at 30 s (magenta), 10 s (blue), 5 s (green). Vertical dotted lines indicate the filter frequency. The black horizontal dotted line indicates the noise level of a Nortek Vector ADV configured to measure  $\pm 4$  m/s. The shaded region indicates the range of spectra presented herein ( $0.002 < \text{tke} < 0.03 \text{ m}^2/\text{s}^2$ ,  $1\text{e-}5 < \varepsilon < 5\text{e-}4 \text{ W/kg}$ ).



738 FIG. 7. Time series of tidal velocity at Admiralty Head from TTM measurements (black), and an acoustic  
 739 Doppler profiler (red). The profiler measurements—taken at the same depth as the ADV on the TTM—were  
 740 contaminated by acoustic reflection from the strongback fin when it was inline with one of the profiler’s beams.  
 741 Note that the vertical scale on the three axes vary by more than an order of magnitude; the small ticks in A and  
 742 B are equivalent to the ticks in C.



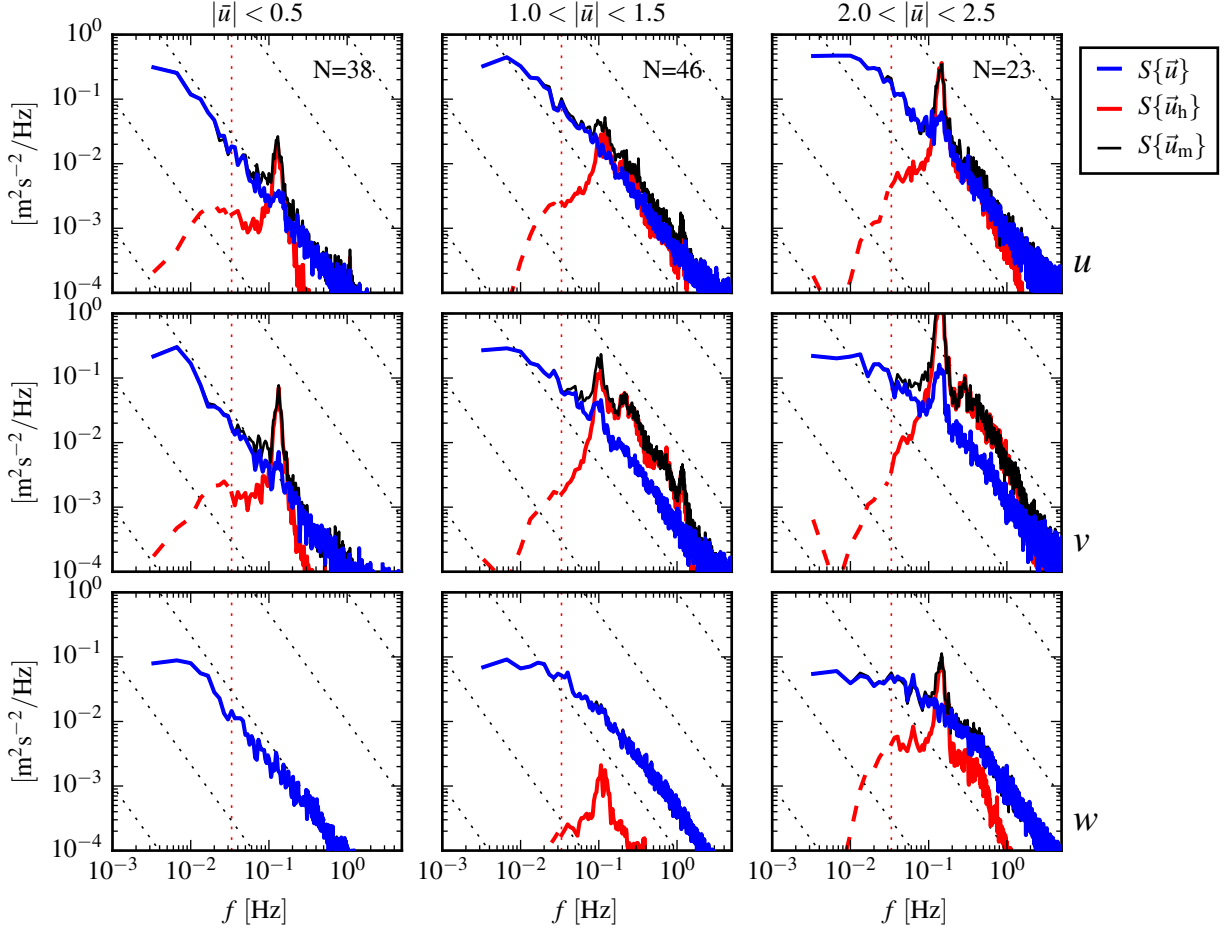


FIG. 8. Turbulence spectra from the June 2014 TTM deployment. Each column is for a range of streamwise velocity magnitudes (indicated at top). The rows are for each component of velocity (indicated to the lower right of the right column). The uncorrected spectra are in black and the corrected spectra are blue, and the spectra of ADV head motion,  $\vec{u}_h$ , is red (also indicated in the legend). The vertical red dotted line indicates the filter frequency applied to the IMU accelerometers when estimating  $\vec{u}_h$ ; below this frequency  $S\{\vec{u}_h\}$  is plotted as a dashed line. Diagonal black dotted lines indicate a  $f^{-5/3}$  slope. The number of spectral ensembles,  $N$ , in each column is indicated in the top row.

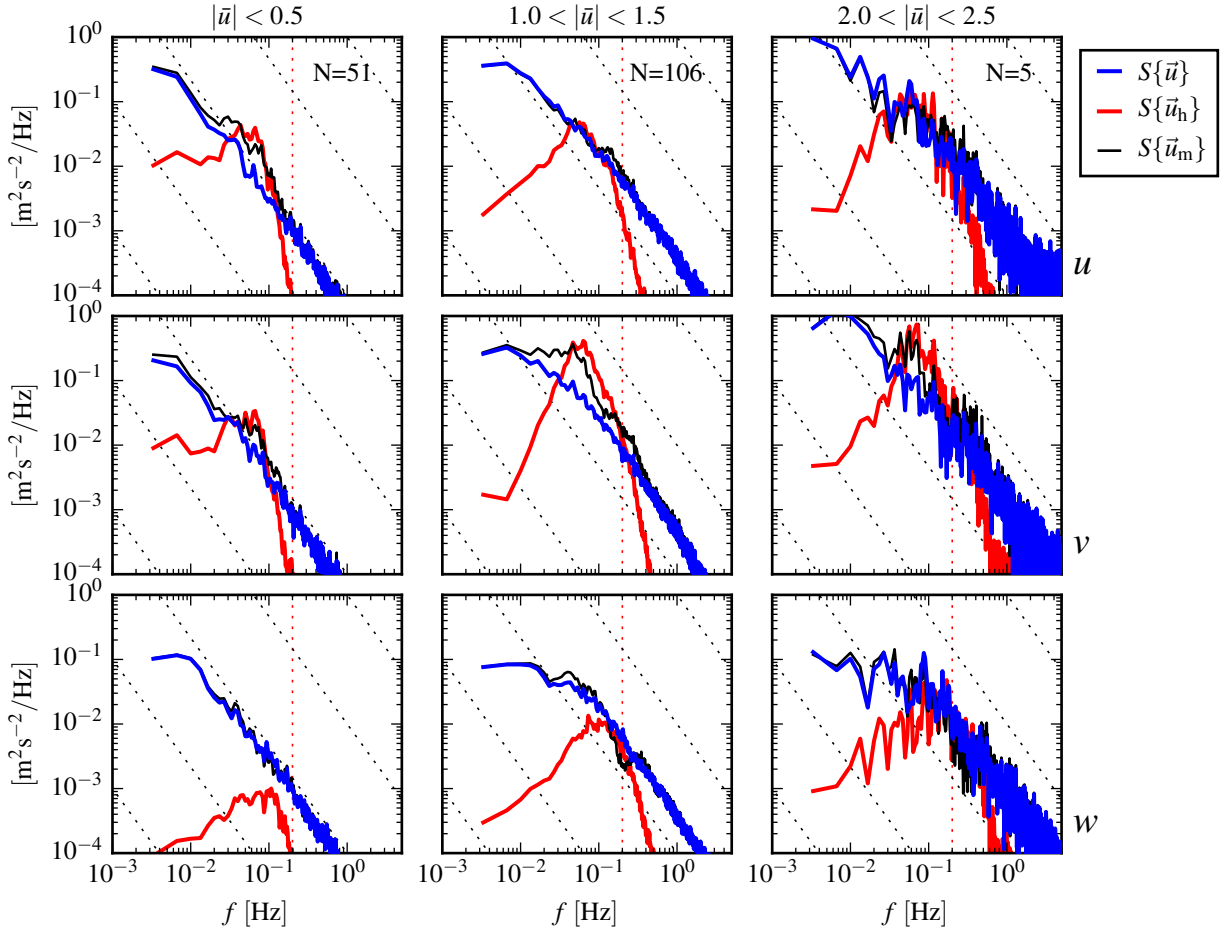


FIG. 9. Turbulence spectra from the StableMoor buoy. The axes layout and annotations are identical to Figure 8, except that  $S\{\vec{u}_h\}$  is plotted as a solid line at all frequencies because it is measured at all frequencies.

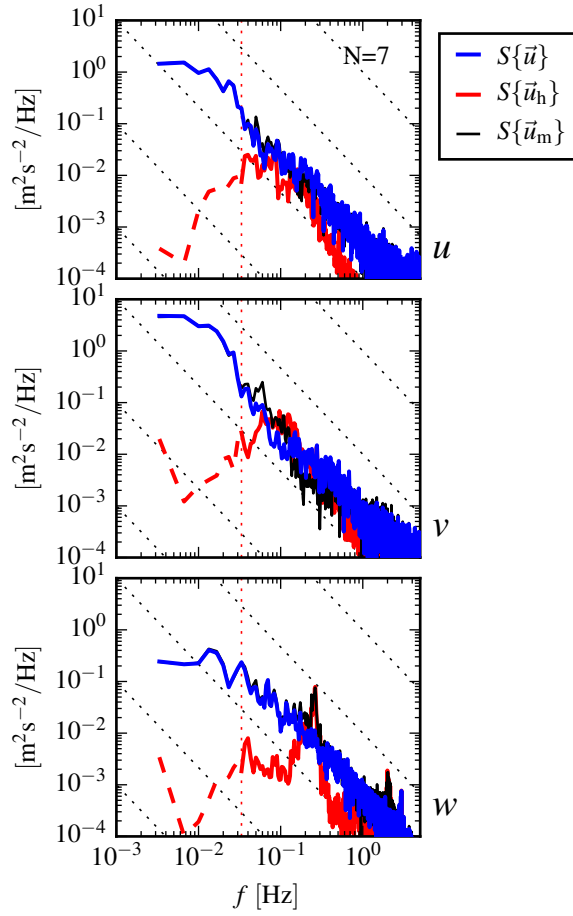


FIG. 10. Turbulence spectra from the turbulence torpedo during a 35-minute period when the mean velocity was 1.3 m/s. Annotations and line colors are identical to Figure 8.

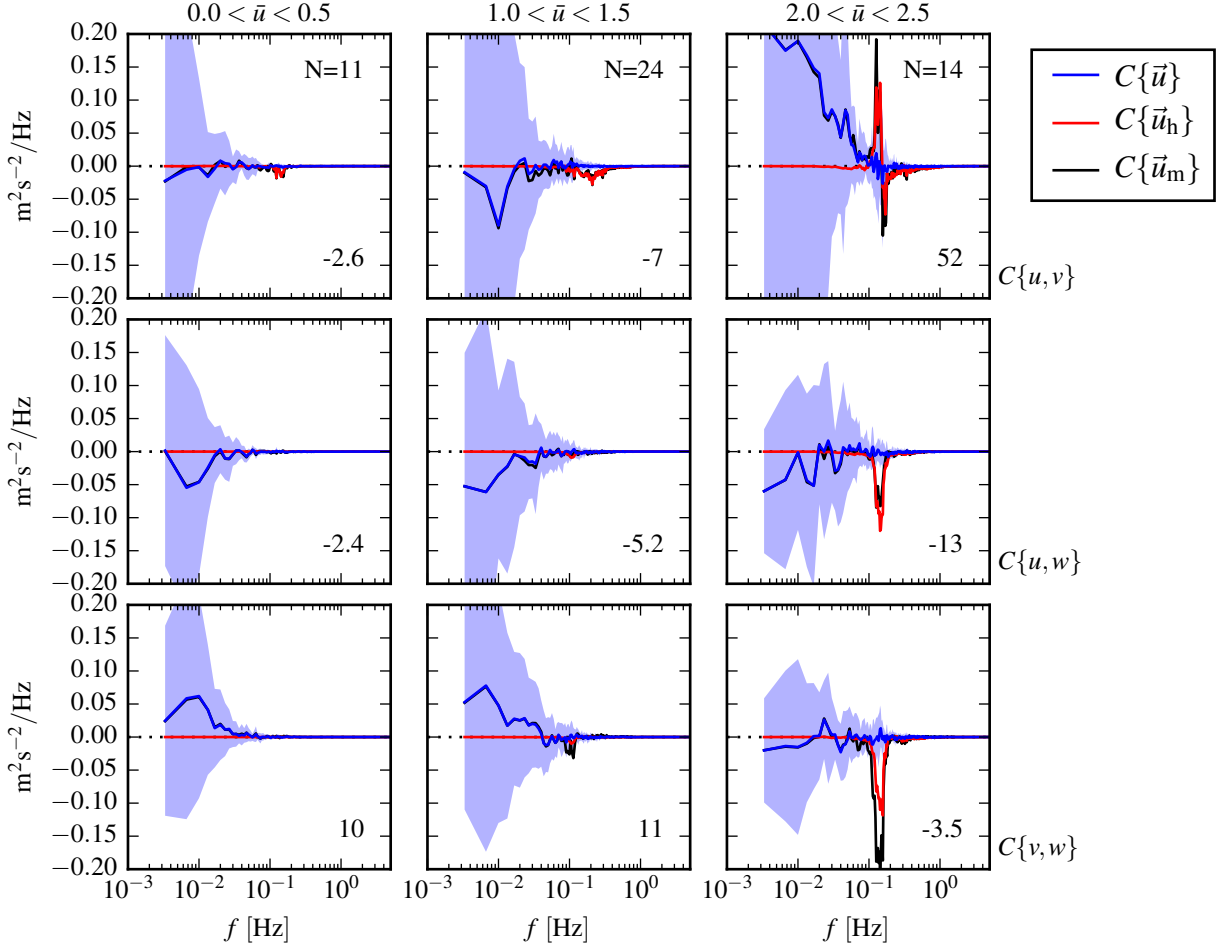


FIG. 11. The real part of the cross-spectral density between velocity components measured by the TTM. The upper row is the  $u$ - $v$  cross-spectral density, the middle row is the  $u$ - $w$  cross-spectral density, and the bottom row is the  $v$ - $w$  cross-spectral density. The columns are for different ranges of the stream-wise mean velocity magnitude (indicated above the top row). The blue line is the cross spectrum between components of motion-corrected velocity, the red line is the cross spectrum between components of head-motion, and the black line is the cross spectrum between components of uncorrected velocity. The light blue shading indicates one standard deviation of the  $C$  for the motion-corrected cross-spectral density.  $N$  is the number of spectral ensembles in each column. The number in the lower-right corner of each panel is the motion-corrected Reynold's stress (integral of the blue line) in units of  $1\text{e-}4 \text{ m}^2\text{s}^{-2}$ .

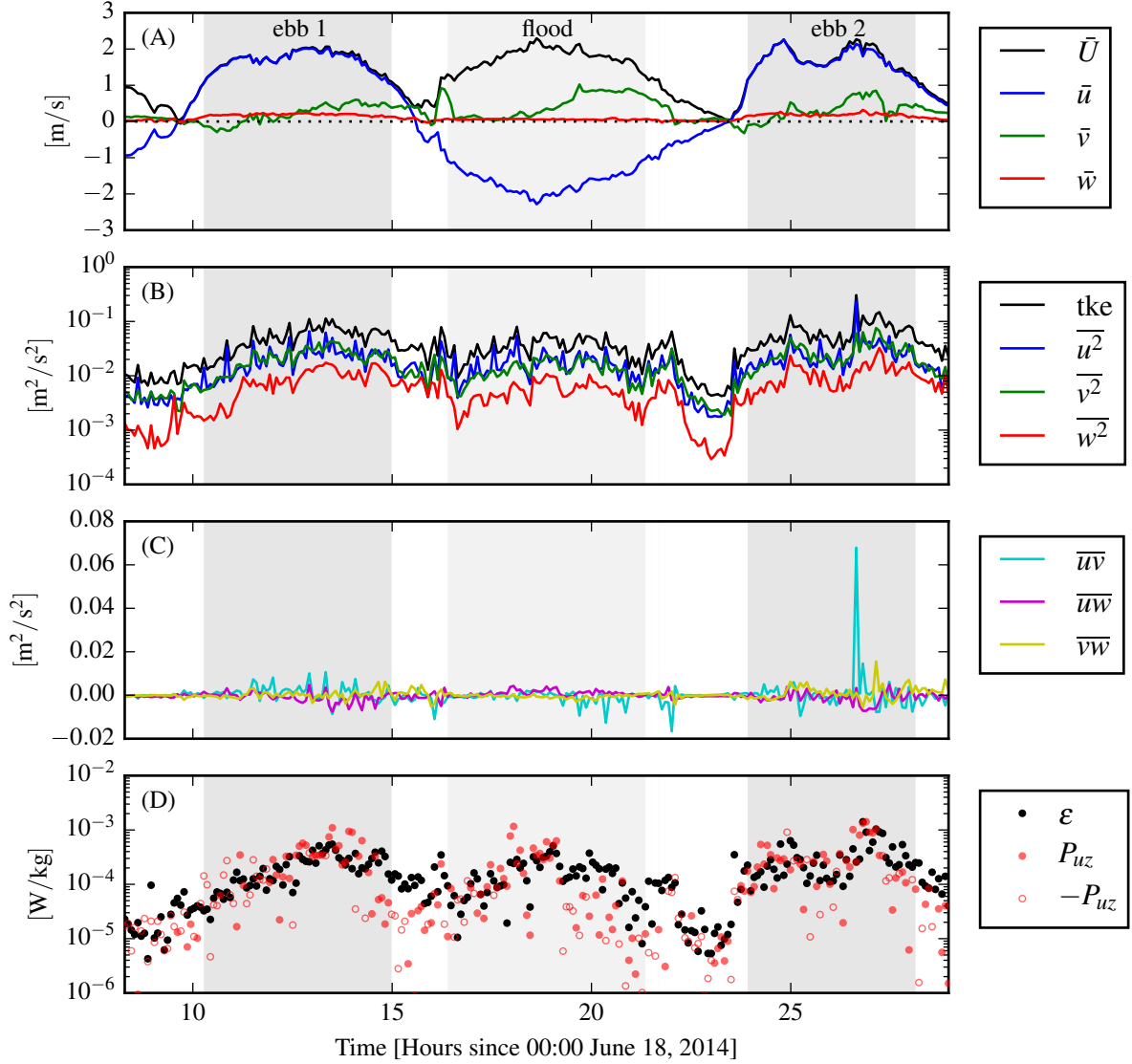


FIG. 12. Time series of mean velocities (A), turbulence energy and its components (B), Reynold's stresses (C), and turbulence dissipation rate (D) measured by the TTM during the June 2014 deployment. Shading indicates periods of ebb ( $\bar{u} > 1.0$ , grey) and flood ( $\bar{u} < -1.0$ , lighter grey).

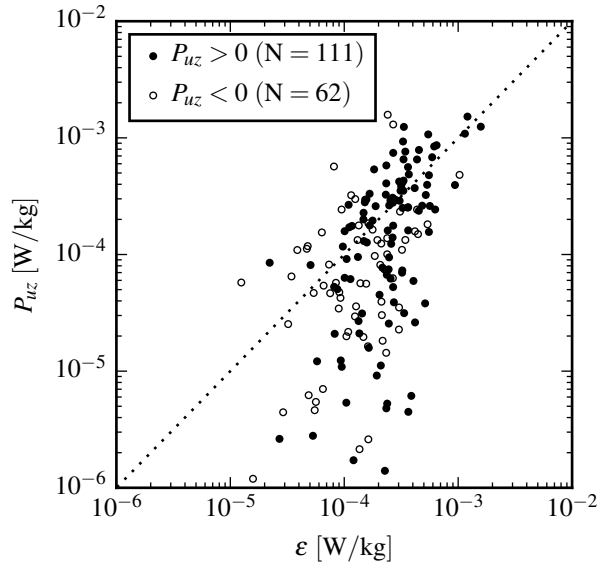


FIG. 13.  $P_{uz}$  vs.  $\varepsilon$  during the June 2014 TTM deployment for values of  $|u| > 1$  m/s. Values of negative production are indicated as open circles.

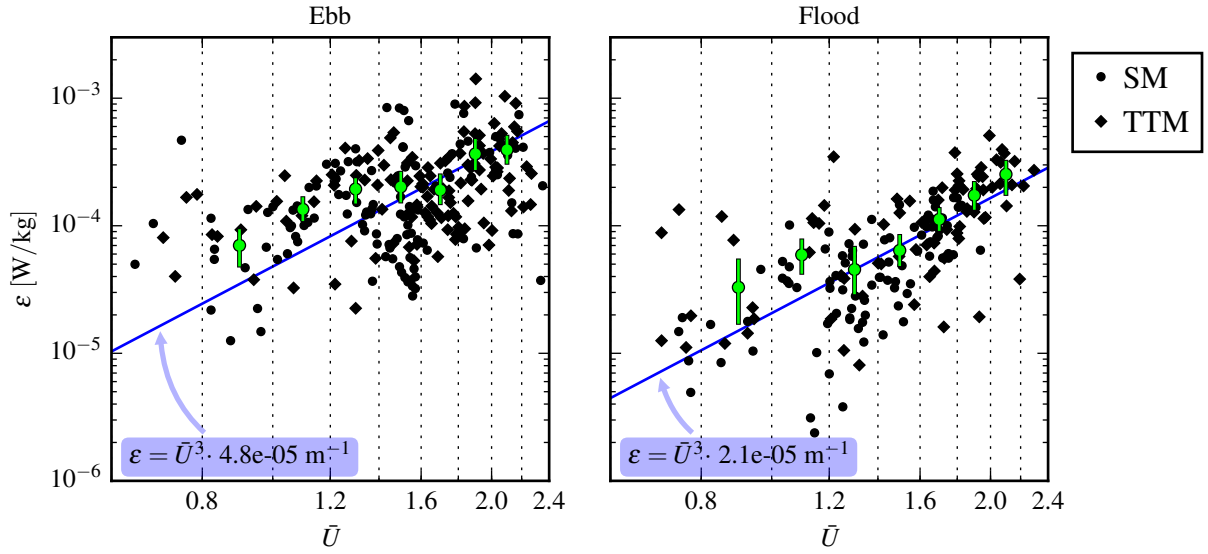


FIG. 14. A log-log plot of  $\varepsilon$  versus  $\bar{U}$  for the June 2014 TTM (diamonds) and May 2015 StableMoor (dots) deployments, during ebb (left) and flood (right). Black points are 5-minute averages. Green dots are mean values within speed bins of  $0.2 \text{ m s}^{-1}$  width that have at least 10 points (50 minutes of data); their vertical bars are 95% bootstrap confidence intervals. The blue line shows a  $U^3$  slope, wherein the proportionality constant (blue box) is calculated by taking the log-space mean of  $\varepsilon/U^3$ .

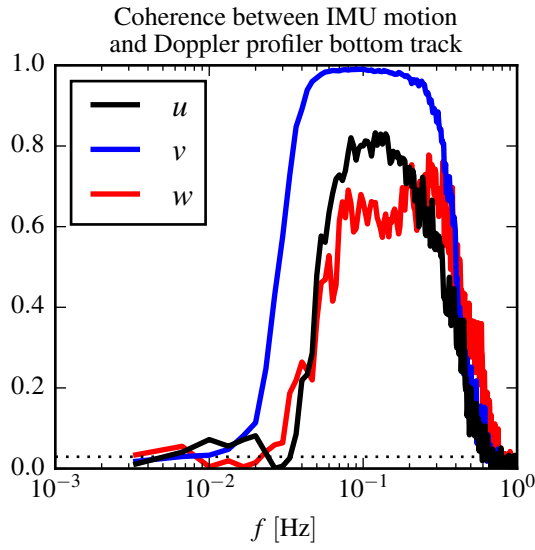


FIG. 15. Coherence between IMU-measured motion of StableMoor buoy and ADP bottom-track velocity for  $1.0 < \bar{U} < 1.5$ . The horizontal dotted line indicates the 95% confidence level for the 102 spectral windows in this estimate.